Acta Materialia 257 (2023) 119025

Contents lists available at ScienceDirect

Acta Materialia

journal homepage: www.elsevier.com/locate/actamat

Degradation of electrical resistivity of tungsten following shielded neutron irradiation

J.R. Echols [a,b,*], L.M. Garrison [a,c], N. Reid [a,d], C.M. Parish [a], A. Hasegawa [f], A. Bhattacharya [a,b], W. Zhong [a], D. Morrall [a,e], M. Lance [a], Y. Katoh [a]

[a] Materials Science and Technology Division, Oak Ridge National Laboratory, Oak Ridge, TN, USA
[b] UK Atomic Energy Authority, Culham, England, United Kingdom
[c] Commonwealth Fusion Systems, Devens, MA, USA
[d] University of Illinois Urbana Champaign, Champaign, IL, USA
[e] Savannah River National Laboratory, Aiken, SC, USA
[f] Tohoku University, Sendai, Miyagi, Japan

ARTICLE INFO

Keywords:
Tungsten
Grain boundaries
Transport properties
EBSD
Neutron irradiation

ABSTRACT

A major challenge for heat transfer in nuclear materials is to ensure thermal mobility after high amounts of neutron irradiation. Tungsten is widely selected as a heat transfer material in fusion reactors. In metals, thermal conductivity is dominated by electrons' ability to transfer energy. Neutron irradiation generates point defects, clusters, and solid transmutation (e.g.rhenium and osmium in tungsten), which inhibit electron motion. The purpose of this work is to quantify the irradiation-induced change in electron mobility and deconvolute transmutation and microstructural effects on observed changes to electron mobility. Single and polycrystalline tungsten were fast neutron irradiated in the High Flux Isotope Reactor at Oak Ridge National Laboratory to doses between 0.2 and 0.7 displacements per atom (dpa) and temperatures from 500 °C to 1000 °C. Grain growth was observed in all samples. Microstructure and transmutation were quantified. The geometric orientation of samples with elongated grains has been shown to affect electrical resistivity. A mathematical model was developed and used to deconvolute solid-solution transmutation, grain, and temperature-dependent lattice effects on resistivity. At ~0.4 dpa at ~590 °C, the combined resistivity degradation due to voids, vacancies, interstitials, and dislocations is estimated to be greater than the contribution from solid solution *Re* transmutation, which is greater than the contribution from grain boundaries. At doses of ~0.7 dpa at ~750 °C, solid solution *Re* contributions are greater than all other effects combined. This work establishes a basis to predict the effects of irradiation temperature and transmutation on thermal properties of tungsten and highlights the importance of irradiation temperature.

1. Motivation and introduction

Development of fusion power plants faces the technical obstacles of effective plasma containment and survivable materials. The challenge of materials, in deuterium-tritium fusion, is dominated by a high fluence of 14.1 MeV neutrons, which provide significant damage to the first wall of materials the neutrons encounter following the fusion reaction. The divertor of a tokamak power plant, which captures and transfers the heat of the reaction, is expected to be subject to 20–30 displacements per atom (dpa) of neutron damage over a reactor lifetime [1]. Radiation-induced defects and transmutation will degrade the thermal conductivity of the divertor materials, which can severely impact the components' ability to effectively remove heat produced in the fusion reactor.

The thermal conductivity of metals depends primarily on the motion of electrons and phonons but becomes less efficient due to scattering of electrons and phonons. The electronic contribution to the thermal conductivity, κ_e, is dominant in metals and often approximated by the Wiedemann–Franz law:

$$\frac{\kappa_e}{\sigma} = LT \tag{1}$$

* Corresponding author at: Technology Department; United Kingdom Atomic Energy Authority; Culham Science Centre; Abingdon OX14 3DB, United Kingdom.
E-mail address: John.Echols@ukaea.uk (J.R. Echols).

https://doi.org/10.1016/j.actamat.2023.119025
Received 22 August 2022; Received in revised form 14 April 2023; Accepted 18 May 2023
Available online 13 June 2023
1359-6454/© 2023 Published by Elsevier Ltd on behalf of Acta Materialia Inc.

Where σ is electrical conductivity, T is temperature, L is the Lorenz number. The actual proportionality factor L deviates from the theoretical Lorenz number depending on temperature and material. Tungsten or its alloys are the presumptive material for the divertor- the heat removal component - in many paths for fusion [1,2]. Tungsten possesses an unusually high L, typically reported as $3.2 \bullet 10^{-8}$ $W\Omega K^{-2}$ [3] where W is Watts, Ω is Ohms, and K is degrees Kelvin. There is disagreement in the literature as to the extent of the phononic contribution to the thermal conductivity of tungsten [3–7], with the estimated ranges between 25% [3,7] and less than 1% [8] of the total thermal conductivity. The majority of literature on tungsten, however, assumes negligible phonon contribution [9,10]. The motion of electrons, therefore, is expected to dominate the material's ability to transfer heat both prior to and following irradiation. Therefore, we measured electrical resistivity to provide direct insight to the degradation of the electron transport.

Resistivity degradation measurements in lattice-damaged and/or transmuted tungsten exist mainly in the context of determining the temperature effects on lattice recovery [11–14]; e.g. temperatures where vacancy mobility becomes high enough to annihilate significant Frenkel-pairs on small timescales. Only limited work exists on neutron irradiated changes to resistivity at neutron dose levels above 0.1 dpa [15–17]. A more complete understanding of the changes to electron mobility in fusion-relevant tungsten irradiation is necessary. This understanding not only allows us to evaluate whether the Wiedemann–-Franz law holds under irradiation, but also impacts component lifetime and design criteria, and has the potential to reveal design spaces for optimizing tungsten and tungsten alloy thermal properties for fusion-relevant radiation damage. Here, fusion-relevant neutron spectrums are defined as having a higher fast neutron to thermal neutron ratio than what is generated in reactors such as the High Flux Isotope Reactor (HFIR). This allows more accurate simulation of neutron damage for fusion scenarios which will be dominated by 14.1 MeV neutrons.

The Plasma Facing Component Evaluation by Tritium, Plasma, Heat, and Neutron Irradiation Experiments (PHENIX) project [18] presents an ideal opportunity to evaluate electrical resistivity of irradiated tungsten microstructures and alloys. PHENIX is the latest in a series of U.S.-Japan collaborations for the technological assessment of plasma facing components for demonstration power plants. One of the main goals of this experiment is to understand the thermomechanical properties of tungsten irradiated with a transmutation-to-dpa ratio relevant to fusion plasma facing components (PFCs), which is accomplished through the use of an irradiation shield made of gadolinium [18].

Two key, quantifiable factors to determining electron mobility following irradiation are (1) the amount and distribution of transmutation that has occurred (W to *Re* and *Re* to Os) and (2) microstructural changes to the lattice including defects and any larger-scale microstructural evolution. By measuring the electrical resistivity of unirradiated/irradiated tungsten with varying levels of transmutation and thermal recovery some decoupling of these factors can be achieved. Therefore, the purpose of this work is to deconvolute and determine electrical resistivity changes (both in matrix and at grain boundaries) attributable to:

- Transmutation
- Atomic displacement damage
- The temperature and dose-dependent evolutions of radiation damage and segregations

Secondary to these purposes, this work also aims to test the Wiedemann–Franz law in neutron irradiated tungsten.

2. Methods and materials

2.1. Materials

A variety of single-crystal and polycrystalline tungsten/tungsten alloy samples were irradiated in the PHENIX campaign [19,20]. The materials which were selected for resistivity testing are summarized in Table 1. The selected materials include commercial varieties of single and polycrystalline tungsten (SCW and PCW, respectively), a variety of grain sizes/elongation, and three samples with *Re* or Re+K as alloying elements to W. W-Re alloys are under consideration as a more-ductile alternative to pure W and have the added benefit of approximating transmutation conditions of higher doses than actually experienced. K-doped W-Re has the potential to improve tensile and creep strength. Fig. 1 shows SEM images of a subset of samples which were cut from the same parent block of material in 3 different directions. Although the material arrived with no indication of the longitudinal (L), short transverse (S), and long transverse (T) directions, reasonable assumptions can be made as to these directions from the SEM images. The assumed planes are also indicated in Fig. 1 and Table 1.

Prior to irradiation, samples were machined into 3 mm diameter by 0.5 mm thick disks, first by cutting with electrical discharge machining, then by grinding/polishing to an 800 grit finish to remove contamination and artifacts from the cutting process. The SCW material was more sensitive to machining defects, so the cut surface had to be ground and polished deeper than the PCW to produce a surface more representative of the bulk material. Finally, samples were engraved with a material specific, two symbol code and sample numbers.

2.2. Irradiation conditions

The HFIR at Oak Ridge National Laboratory (ORNL) provides a high flux of neutrons, allowing for rapid turnaround materials testing. However, the reactor has a much higher flux of thermal neutrons than what is expected in future fusion reactors [21,22]. The capsule irradiated in this campaign, RB-19J, was designed to limit thermal neutron exposure by utilizing a thermal shield made of Gd metal surrounding the specimen regions. The thermal flux is expected to be reduced by 1.5–2 orders of magnitude compared to HFIR's normal spectrum [23]. The intended effect from this is to achieve a thermal-to-fast neutron ratio more similar to a fusion spectrum. One important change from this is the reduction of the tungsten transmutation-to-dpa ratio from as high as 50:1 (at%) to nearly 1:1 [23,24]. Fig. 2 shows a direct comparison the transmutation-to-dpa ratio for RB-19J alongside upper and lower estimations of fusion-reactor transmutation calculated from Noda [25] and Sawan [26], respectively. Full information on the design of the capsule is documented in [27].

The divertor will experience an incredibly wide operational temperature window between the plasma-facing side and the coolant side. Several steady state designs require temperatures more than 2000 °C at the plasma facing side, dropping to several hundred degrees on the coolant side [28,29]. Therefore, the PHENIX project was designed to test W at three different fusion-relevant temperature regions which are approximated as the 500 °C, 800 °C, and 1200 °C. The RB-19J capsule had three sub-capsules, each designed for one of these temperatures, and over 1300 samples were ultimately irradiated.

Specimens evaluated here experienced a calculated irradiation temperature range of 550 °C to 1000 °C with calculated DPA values ranging from 0.30 to 0.71. DPA was calculated based on the work of Sawan [26] from fast neutron flux. This flux was estimated by an in-house HFIR code which has been shown to accurately predict neutron flux with 87%−99.5% accuracy [30]. Irradiation occurred over the course of 4 cycles (average cycle length of 24.5 days) in HFIR The irradiation temperature and DPA of each sample is shown with their results in Table 2.

Temperatures in the irradiation capsules were calculated with a combination of active thermocouple measurement (monitored during irradiation at discrete locations), passive SiC thermometry (determined following irradiation [31]), and thermal modeling of the RB-19 J capsule. In the highest temperature subcapsule, failure of thermocouples midway through irradiation resulted in greater temperature uncertainty

Table 1
Summary of tungsten varieties investigated in this work. Elemental quantification on the pure tungsten samples was performed by glow discharge mass spectrometry prior to irradiation. W-*Re* alloys had quantification performed with inductively coupled plasma atomic emission spectroscopy.

Material Code	Description	Single or Poly-crystalline	W (at%)	*Re* (at%)	K (ppm)	Make
AT	Sample face in the T x S plane	Poly	99.998	–	–	ALMT
BT	Sample face in the L x T plane	Poly	99.998	–	–	ALMT
CT	Sample face in the L x S plane	Poly	99.998	–	–	ALMT
UE	Single crystal w/ surface plane (110)	Single	99.999	–	–	Goodfellow
41	W-3%*Re*, rolled 80%	Poly	97	3	–	ALMT
70	K-doped W-3%*Re*, rolled 80%, recrystallized at 1500 °C	Poly	97	3	28	ALMT
80	K-doped W-3%*Re*, rolled 80%	Poly	97	3	28	ALMT

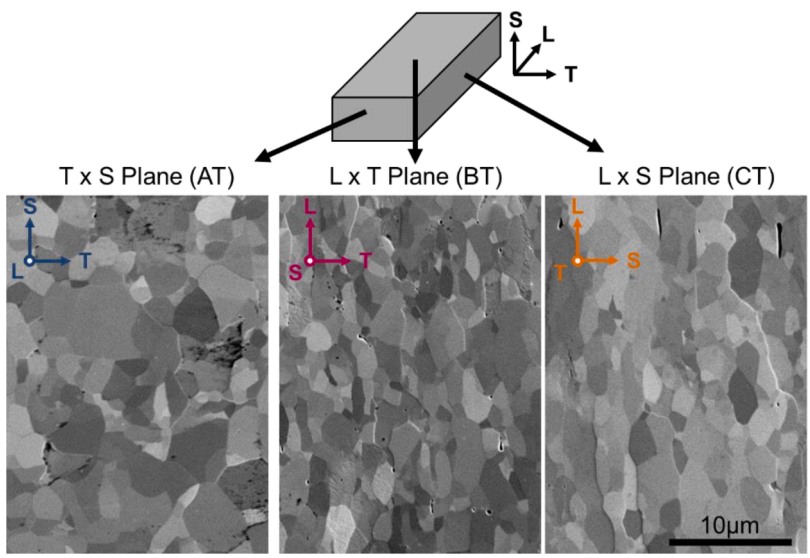

Fig. 1. Microstructure of and relationship to rolling direction for PCW samples. Relationships between the longitudinal (L), short transverse (S), and long transverse (T) directions are indicated.

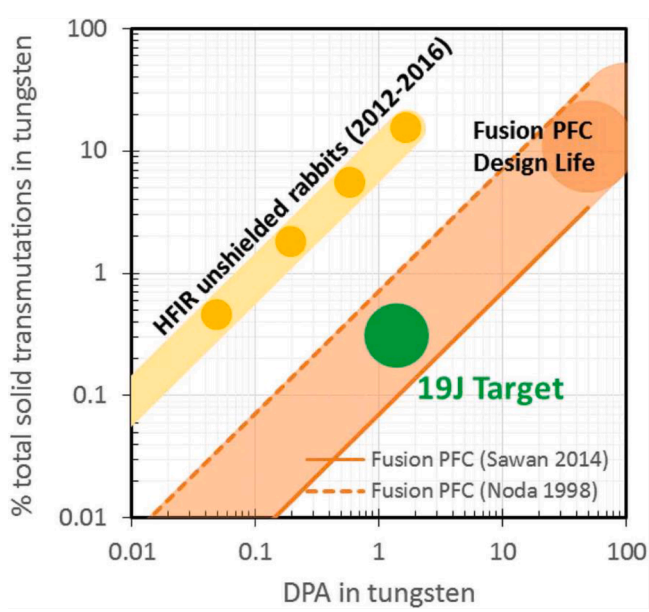

Fig. 2. Expected irradiation profile from the 19-J capsule [23].

for those samples. Out of an abundance of caution, these samples' temperatures are listed with an uncertainty of ±100 °C based on best practices developed in earlier campaigns and noted in the results section.

2.3. Reaction layer removal

A thin reaction layer was discovered on some samples irradiated at higher temperatures. The samples were in graphite holders and had thin graphite spacers between each sample during irradiation. All components and samples were cleaned with alcohols prior to irradiation and mixes of high purity Ar and He were used as the fill gas in the capsule. Scanning electron microscopy (SEM) and energy-dispersive x-ray spectroscopy (EDS) of this layer suggest oxide and/or carbide formation on the sample surfaces to a maximum observed depth of 50 μm, as seen in Supplemental Fig. 1. To avoid measuring the combined resistivity of the film and bulk, samples from the two higher temperature capsules were lightly polished on the lead contact side prior to testing (See Supplemental Fig. 1). The final thickness after polishing was used to calculate resistivity and the resistivity testing device was confirmed to give accurate resistivity regardless of sample thickness on unirradiated tungsten.

2.4. Resistivity testing

Nondestructive, miniaturized resistivity testing equipment was designed and implemented at ORNL for 3 mm diameter x 0.5 mm thick samples. Fig. 3 shows a diagram of the resistivity tester developed for this work. The sample is held steady by a clamp in a non-conductive fixture the contacts are small round points of copper touching the surface of the sample. The device passes a current across the material and measures the voltage drop over a known length.

The resistivity of the measured material is dependent on upon the geometry tested. For the 3 mm disk tester, the relationship is as follows [32]:

Table 2
Grain sizes and irradiation conditions for selected specimens from EBSD data shown in Fig. 4.

Sample Face (ID)	Irradiation Temp (°C)	Dose (dpa)	N Grains	Mean Area (μm^2)	Mean Maj Diameter (μm)	Mean min Diameter (μm)
T x S (AT no irrad)	–	0	12,209	18.2	2.1*	2.1*
L x T (BT no irrad)	–	0	14,930	5.6	1.7	0.8
L x S (CT no irrad)	–	0	32,853	7.1	2.0	0.8
L x S (CT03)	550	0.29	27,633	7.6	2.2	0.8
L x S (CT06)	870	0.74	26,072	8.3	2.2	0.9
L x S (CT07)	990	0.71	2466	345	11.9*	11.9*
SCW (UE06)	990	0.70	–	–	–	–

* Equiaxed grains on average.

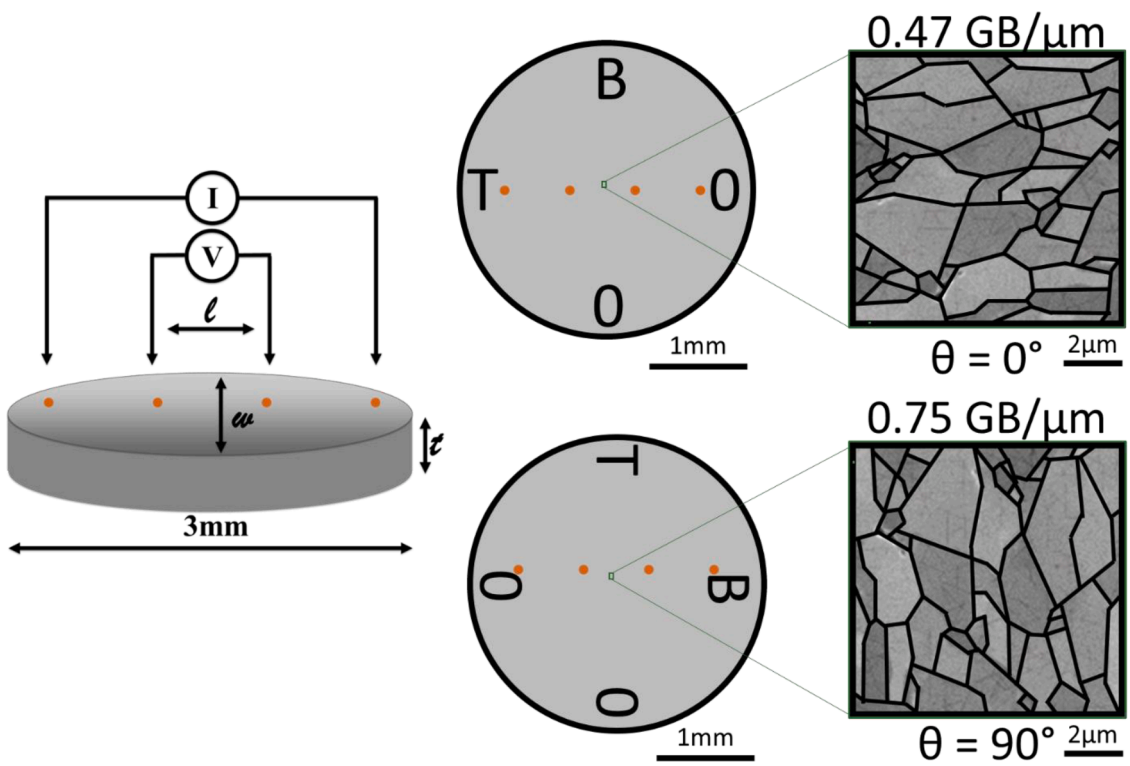

Fig. 3. Schematic of resistivity measuring apparatus with copper contact locations shown in orange. Rotating a sample with elongated grains changes the GB density in the direction of the current flow. The grains on the right of the image are one example taken from a sample but simplified as a drawing to illustrate how the rotation of the sample in the fixture changes how the grains are oriented relative to the measurement probes.

$$\rho = \frac{V}{I} \cdot t \cdot C.F. \tag{2}$$

Here again, ρ is the resistivity, V is the measured voltage drop across the middle two probes, I is the current passed through the sample from the outer two probes, t is the minimum measured sample thickness, and C.F. is a conversion factor calculated from the length and width of the individual samples in a process described fully by Logan [32]. For a circular sheet sample with insulated edges, C.F. is calculated as:

$$C.F. = \frac{\pi}{\ln(2) + \frac{1}{2}\ln\left(\frac{\left[1-\left(\frac{2a}{d}+\frac{S}{d}\right)\left(\frac{2a}{d}-\frac{3S}{d}\right)\right]\left[1-\left(\frac{2a}{d}-\frac{S}{d}\right)\left(\frac{2a}{d}+\frac{3S}{d}\right)\right]}{\left[1-\left(\frac{2a}{d}-\frac{S}{d}\right)\left(\frac{2a}{d}-\frac{3S}{d}\right)\right]\left[1-\left(\frac{2a}{d}+\frac{S}{d}\right)\left(\frac{2a}{d}+\frac{3S}{d}\right)\right]}\right)} \tag{3}$$

Where d is the diameter of the measured disk, S is the distance between each probe (0.61 mm in our custom fixture), and a is the distance between the center-point of the 4-probe system and the center point of the disk. In this case, a is 0, which simplifies the expression to:

$$C.F. = \frac{\pi}{\ln(2) + \frac{1}{2}\ln\left(\frac{\left[1+\left(\frac{S}{d}\right)\left(\frac{3S}{d}\right)\right]^2}{\left[1-\left(\frac{S}{d}\right)\left(\frac{3S}{d}\right)\right]^2}\right)} \tag{4}$$

Because the diameter of each sample differed slightly, this conversion factor was calculated separately for each sample. Sample diameter and thickness were measured thrice with a micrometer and averaged for resistivity calculation. Voltage measurements were performed on a Keithley Model 182 Sensitive Digital Voltmeter. The current source was provided with a Keithley Model 237 High Voltage Source Measure Unit. Resistivity testing was performed between 20 °C and 24 °C with a minimum of 5 (15 max) measurements performed on each sample or each rotation condition. Samples which were rotated had measurements taken at 45° intervals. Resistivity values were then normalized to 20 °C for accurate comparison. Sources of experimental error include the possibility of imprecise rotation angle, which was done by hand with the aid of fiduciary marks and protractor and the possibility of poor sample contact due to possible EDM damage on the sample surface. General test procedures for electrical resistivity testing on metals are given in ASTM B 193-20, Standard Test Method for Resistivity of Electrical Conductor Materials [33].

2.5. Thermal diffusivity

Thermal diffusivity measurements were performed on irradiated and unirradiated SCW samples using a xenon flash and following the

procedures from [34] (where PCW results are reported), including the use of graphene spray sold as 'JA007159: Black coating agent for LFA on very thin specimen' from NETZSCH Japan. These measurements were performed on post-test tensile grips of SSJ2 geometry, which have a thickness of 0.5 mm. While the electrical resistivity measurements are performed with the current passing parallel to the disk surface, the thermal diffusivity instrument measures in the perpendicular direction, which is through the thickness of the sample. A NETZSCH LFA-467 HT was used to for the thermal diffusivity measurements. The device was evacuated to $<4 \times 10^{-4}$ Torr, and measurements were taken between room temperature and up to 800 °C, depending on the maximum irradiation temperature. Heating was performed at a rate of 5 °C per minute with 5 measurements taken at each 50 °C interval upon heating and 3 measurements taken at each 100 °C interval on cooling.

2.6. Microscopy

Electron and Electron Backscatter Diffraction (EBSD) micrographs were taken on a TESCAN MIRA3 Scanning Electron Microscope (SEM) with an advanced Oxford Symmetry EBSD system. Compositional analyses were acquired on an electron microprobe (JEOL 8200) equipped with 5 tunable wavelength dispersive spectrometers. The accelerating voltage was set to 25.0 kV and the beam current was 50.0 nA. Elements were acquired using LiF analyzing crystals for W lα, Re lα, and Os lα. Pure standards were used to calibrate all elements except for Os for which the average intensities of Re lα and Ir lα were used to create a virtual standard. Unknown and standard intensities were corrected for deadtime. Standard intensities were corrected for standard drift measured between the beginning and end of the run. Interference corrections were applied to Re for interference by W and both W and Re for Os.

3. Results

3.1. Microstructure and composition

3.1.1. Grain structure

EBSD micrographs for the three sample orientations are shown in Fig. 4 (with statistics in Table 2), alongside L x S orientation samples from three irradiation conditions. A single-pass cleaning procedure was performed on the EBSD data (using the OIM Analysis software by EDAX) to generate accurate grain size measurements in the data and is reflected in the images in the figure. Grain diameters and areas are shown for all measured samples in Table 2. Recrystallization and grain growth are observed in the 990 °C, 0.71 dpa specimen. Visually, the 550 °C, 0.29 dpa and 870 °C, 0.70 dpa specimens' grains look the same as the unirradiated sample. To statistically try to determine if grain growth occurred between the irradiation conditions, a 2-sample Kolmogorov-Smirnov test was performed on the grain areas to determine if the populations could be considered identical. Results of this test can be seen in Table 3.

The p-values for all tests indicate that we can reject the null hypothesis and conclude that all populations of grain area are distinct. Quantifiable grain growth has occurred at all irradiation conditions. For the lower temperatures, we believe this is most likely irradiation-

Table 3
Kolmogorov-Smirnov test results with associated p-values for the grain area of representative samples.

	550 °C, 0.29 dpa (CT03)	870 °C, 0.70 dpa (CT06)	990 °C, 0.7dpa (CT07)
Unirradiated (CT no irrad)	0.07 $p = 10^{-58}$	0.15 $p = 10^{-272}$	0.90 $p = 0$
550 °C, 0.29 dpa (CT03)	–	0.09 $p = 10^{-98}$	0.90 $p = 0$
870 °C, 0.70 dpa (CT06)	–	–	0.89 $p = 0$

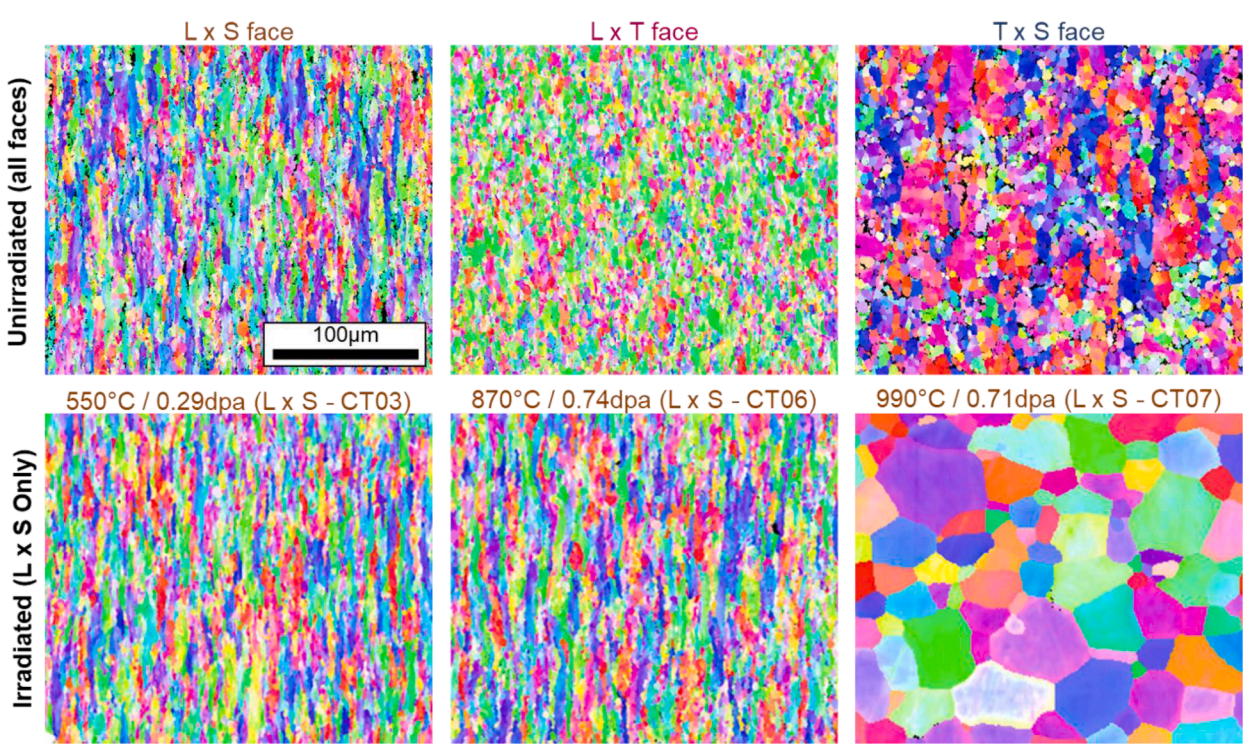

Fig. 4. Inverted Pole Figure maps (z-direction) of unirradiated (top) and irradiated (middle) PCW samples. Histograms of grain area are shown for irradiated specimens in Supplemental Figure 2, indicating minor grain growth below the highest temperature irradiation.

induced. In the highest temperature irradiation, we observe large growth and/or recrystallization - likely well below what we would expect for unirradiated annealing for this irradiation length [35]. Practically, we consider grain distributions similar for irradiations below 870 °C. Large amounts of recrystallization and/or grain growth is only considered for samples irradiated at temperatures >870 °C. Histograms comparing the grain sizes are shown in Supplemental Fig. 1. Based on the results of the CT samples, we postulate that the AT and BT samples may also have had minimal grain growth for irradiation temperatures <870 °C, and potentially recrystallized at higher irradiation temps. We discuss the resistivity results with that in mind.

Measurements of the angular dependence of resistivity for six specimens are shown in Fig. 5. Unirradiated and irradiated B-series PCW (which does not have equiaxed grains relative to the current for different rotations in the resistivity fixture) show resistivity that oscillates with measurement angle. However, samples which are likely recrystallized (BT08), equiaxed relative to the current (AT01) or have no grains (UE06), do not oscillate, meaning the oscillatory behavior results from the effects of grain boundaries (GBs), rather than textural effects. Sine curves fits to the oscillatory data and the amplitude in oscillations might be taken as the GB effect on resistivity.

3.1.2. Elemental composition

Composition was measured by Wavelength-Dispersive Spectroscopy (WDS) for samples of SCW, PCW, irradiated W-Re alloys, and unirradiated W-Re-Os alloys (Table 4). Unirradiated W-Re alloys were measured by inductively coupled plasma - optical emission spectrometry (ICP-OES) by Evans Analytical Group.

Elemental composition samples are distinct from those from which the resistivity measurements were taken. For the WDS samples, 10 distinct sites in the bulk of each sample were measured, and the average transmutation levels are shown alongside a single standard deviation. For the unalloyed samples, EDS maps taken during measurement do not show any resolvable areas of *Re*/Os concentration, and we assume relatively uniform distribution of transmutant elements at WDS-relevant scales (note that segregations such as nanoscale clusters of *Re* and Os observed in [36] and grain boundary segregation observed in [37] would not show up in the larger areas considered by WDS) [36]. For unalloyed specimens, if we also assume linear transmutation rates in this dose regime [10], we calculate a dose: transmutation ratio of 1 dpa: 0.83 *Re* (at%). The R^2 value of our data to this fit is 0.98, giving confidence in this assumption. Pre-alloyed specimens are not expected to exhibit the same transmutation ratio since *Re* continues to transmute to Os.

Table 4
Elemental composition of selected samples measured by WDS. Error represents a single standard deviation in either direction.

Sample Type	Sample ID	Irradiation Temp (°C)	Dose (dpa)	Measured *Re* (at%)	Measured Os (at%)
PCW	AT00	510	0.33	0.23 ± 0.03	0.00 ± 0.00
	AT08	780	0.69	0.57 ± 0.02	0.00 ± 0.01
	AT0G	900	0.66	0.50 ± 0.01	0.00 ± 0.00
SCW	UE03	480	0.26	0.16 ± 0.02	0.00 ± 0.00
	UE0A	830	0.74	0.73 ± 0.02	0.00 ± 0.00
	UE0L	930	0.63	0.49 ± 0.02	0.01 ± 0.01
W-*Re*	5E no irrad	–	–	2.21 ± 0.02 *	–
Alloy	5E00	530	0.27	2.32 ± 0.06	0.10 ± 0.02
	5E01	910	0.74	2.48 ± 0.13	0.30 ± 0.02
	3R no irrad	–	–	0.40 ± 0.01 *	–
	3R01	530	0.28	0.51 ± 0.01	0.00 ± 0.00
W-*Re*-Os	W 3Re 0.7Os	–	–	3.07 ± 0.0	0.69 ± 0.0
Alloy	W 5Re 3Os	–	–	5.35 ± 0.0	3.67 ± 0.0
	W 10Re 5Os	–	–	10.15 ± 0.08	5.35 ± 0.03

* Denotes samples measured with ICP-OES. All other measurements are measured with WDS.

3.2. Resistivity

Measured resistivities and the calculated electronic contribution to the thermal diffusivity, α_e, along with irradiation temperature and dose, are shown in Table 5. For each sample and sample rotation condition, at least 5 measurements were taken, with the average resistivity value and standard deviation reported. Values for α_e were calculated from the Wiedemann–Franz law, assuming negligible effects from density and specific heat capacity changes in irradiated materials and a Lorenz number of $3.2 \bullet 10^{-8}$ $W\Omega K^{-2}$. Samples are color coded by material in the table and some following figures, with T x S orientation PCW in blue, L x T -orientation in pink, and SCW in green. This data, except for the alloy samples, is visualized in Fig. 6 where resistivity is shown against dose for SCW and 2 PCW grain elongation states. Irradiation temperature, which can anneal out lattice defects, is shown with a colorbar and callouts. Notably, the spread in the data for SCW samples is much larger than for

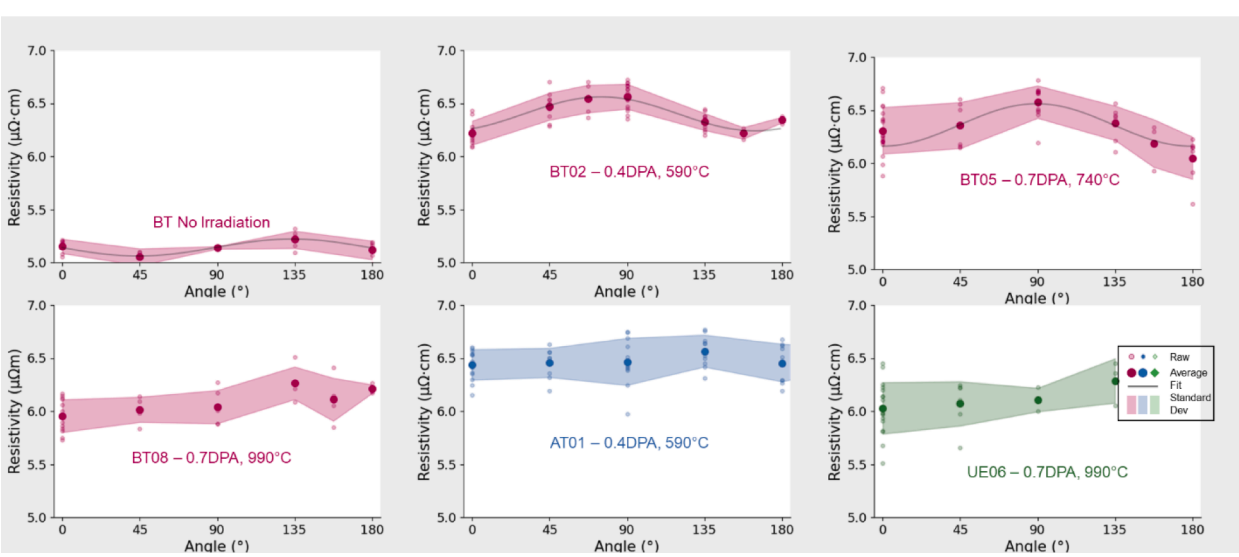

Fig. 5. Resistivity as a function of sample rotation in the fixture during measurement. Fit lines are shown for the top row of samples, which behave in a periodic fashion. Samples shown in the bottom row do not exhibit periodicity. The starting angle, 0°, was arbitrary and therefore not consistent across samples.

Table 5
Irradiation parameters, resistivity, and calculated electronic contribution to the thermal diffusivity (α_e) of selected samples for 20 °C. *Re* percentages are calculated from the WDS data.

Face orientation/ description	Sample ID	Irradiation Temp (°C)	Dose (dpa)	Calculated *Re* (at.%)	Average Resistivity (μΩ•cm)	STDEV (μΩ•cm)	α_e (mm^2/s)
T x S / PCW	AT01	590	0.38	0.32	6.30	0.18	56.2
	AT02	550	0.33	0.27	6.25	0.31	57.1
	AT04	830	0.73	0.61	6.41	0.18	55.7
	AT05	760	0.68	0.56	6.30	0.02	57.5
	AT06	990*	0.70	0.58	5.73	0.17	61.1
	AT07	990*	0.70	0.58	6.39	0.09	56.7
L x T / PCW	BT no irrad	–	0.00	0.00	5.05	0.07	70.6
	BT02	590	0.38	0.32	6.22	0.11	56.7
	BT05	740	0.68	0.56	5.95	0.19	56.8
	BT06	850	0.73	0.61	6.74	0.04	53.8
	BT08	990*	0.71	0.59	5.96	0.15	59.0
L x S / PCW	CT07	980*	0.71	0.59	6.63	0.03	54.6
SCW	UE no irrad	–	0.00	0.00	4.85	0.08	74.7
	UE02	550	0.30	0.25	5.49	0.41	66.0
	UE05	810	0.71	0.59	6.11	0.53	55.6
	UE06	990*	0.70	0.58	6.03	0.09	58.9
W 3% *Re*, Rolled	410F	930*	0.68	3.20	10.1	0.26	35.9
K-doped W 3% *Re*, Recrystallized	700F	980*	0.69	3.20	10.6	0.37	33.7
K-doped W 3% *Re*, Rolled	800F	920*	0.68	3.20	11.0	0.44	32.7

* Denotes best estimate of temperature.

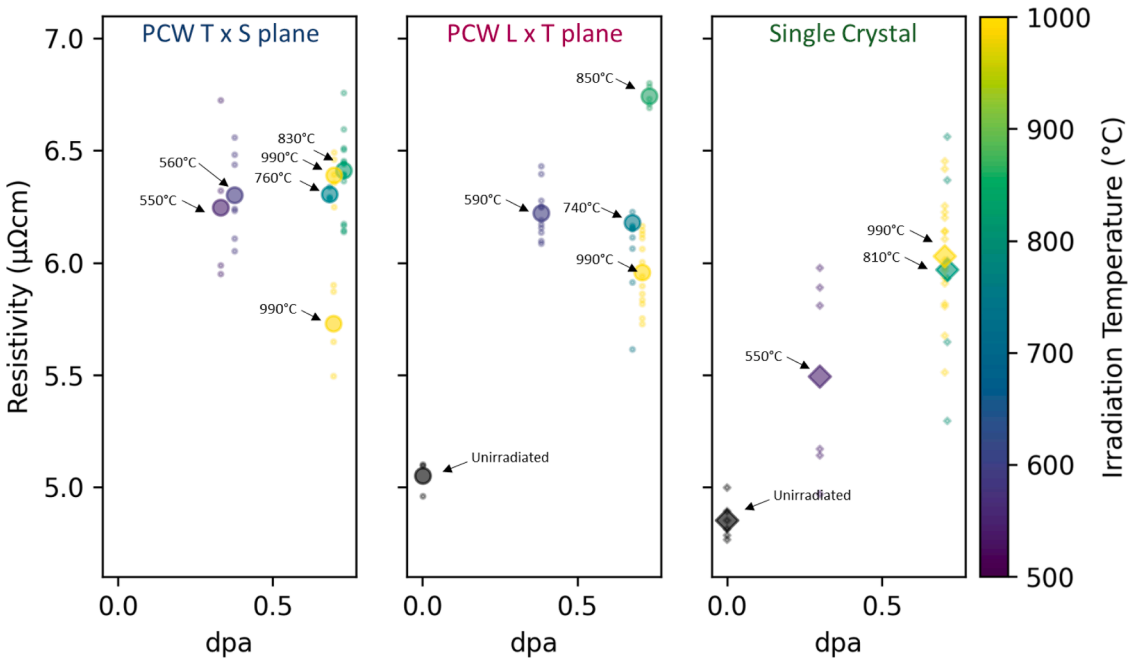

Fig. 6. Resistivity as a function of dose and irradiation temperature for SCW and PCW samples. Large markers denote mean values; small markers are individual measurements.

the PCW. This is attributed to machining artefacts from EDM, which were much more severe on the SCW than the PCW samples and may not have been completely removed during polishing (see Fig. 2 in [38]) – leading to an increased apparent resistivity and variability.

3.2.1. *Thermal diffusivity*

Thermal diffusivity measurements of SCW specimens, with reciprocal linear fits, are shown in Fig. 7. Specimens are half tensile bars from the same irradiation capsules, but different areas of these capsules. Therefore, irradiation conditions are similar, but not identical to, the electrical resistivity specimens. No hysteresis was observed in any of the samples, so it is assumed that the measurement temperature never exceeded the maximum irradiation temperature. Therefore, all individual measurements from both heating and cooling are considered and weighted evenly in the fitting procedure. Comparing the samples irradiated at 830 °C and 930 °C, which have similar dose levels, we can note that there is minimal diffusivity difference. We can conclude from this that there is little temperature effect between these temperatures. The low-temperature irradiation - at significantly less dose - exhibits markedly less diffusivity compared to the high temperature irradiations.

4. Discussion

To model the total resistivity of irradiated tungsten, we should consider lattice resistivity ($\rho_{lattice}$) plus the effects of GBs (ρ_{GB}), solid-solution transmutation ($\rho_{tr.SS}$), transmutant precipitates in the bulk ($\rho_{tr.P}$), transmutant segregation to GBs ($\rho_{tr.GB}$), voids (ρ_{void}), dislocations (ρ_{dis}), vacancies (ρ_v), interstitials (ρ_i), and crystallographic texture (ρ_{tex}).

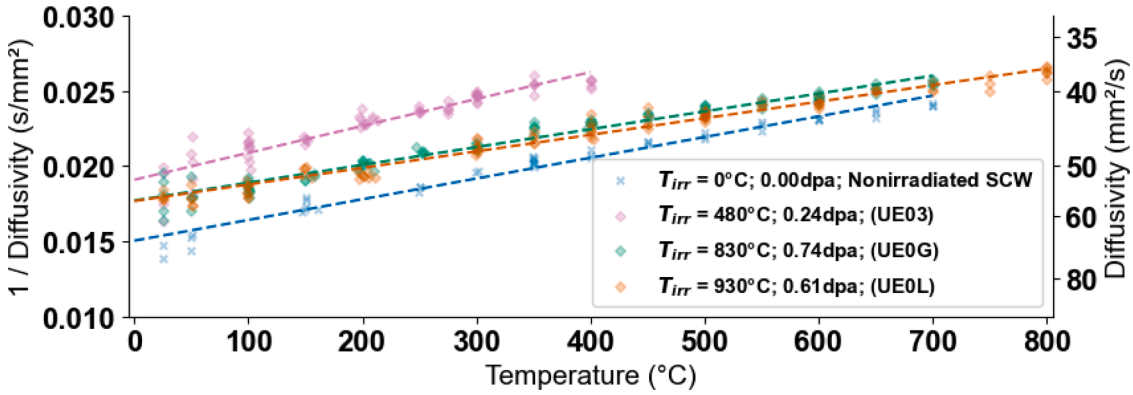

Fig. 7. Measured thermal diffusivity data (with fits) for SCW samples.

According to Matthiessen's approximation rule for electrical resistivity, the total resistivity of a crystalline metallic material can be represented as the sum of the lattice resistivity and these imperfections to the lattice. In the most general form for this situation:

$$\rho_{total} = \rho_{lattice} + \rho_{GB} + \rho_{tr.SS} + \rho_{tr.P} + \rho_{tr.GB} + \rho_{void} + \rho_{dis} + \rho_{v} + \rho_{i} + \rho_{tex} \quad (5)$$

The work of Tanno et al. [16,39]. highlights the extremely large effect expected of transmutant Os (roughly 5x the effect of *Re* as shown in Table 4 of their work). Transmutant Os, however, is not observed in significant quantity in this work. Additionally, there are several recent studies Mergia et al. [40] and Reza et al. [41] provide two recent discussions focusing on void, vacancy, and dislocation effects in irradiated tungsten. Here, we will seek to discuss and expand the understanding of the changes attributable to GBs, transmutant *Re* content, and textural effects. To build necessary context, we will also discuss effects associated with irrtion temperature and evaluate whether the Wiedemann–Franz law holds under irradiation.

4.1. Temperature effects

Recovery of neutron irradiation effects in metals generally follows four distinct stages [11,12,13]. In tungsten, stage III (self-interstitial migration) is divided into two separate regions, the first between 100 and 450 °C, and the second between 450 and 650 °C. Stage IV (vacancy migration) occurs between 650 and 1000 °C. Keyes and Moteff's [11] work shows the relative effect (at doses between 8.5 • 10^{17} and 1.5 • 10^{21} n/cm^2) of each of these recovery stages to be stage III (1) as the most degrading to resistivity, then stage IV, then stage III (2). All materials discussed here were irradiated beyond the first self-interstitial region, and within the second, but not all fell inside the region for vacancy migration. Vacancy density, therefore, is believed to contribute significantly to the resistivity between the low and high temperature samples, while self-interstitials are not. In this context, the high resistivity/low diffusivity of the low-temperature/low dose specimens, when compared to the high temperature/high dose cases, can be understood.

4.2. Comparison between resistivity and diffusivity

Table 6 shows a comparison of calculated electronic contribution to thermal diffusivity from this work alongside fits from measured thermal diffusivity values. Akiyoshi et al.'s [34] measurements are from material from the same irradiation and same parent block of material as this work. In unirradiated specimens, they note a difference of 3 mm^2/s (≈5%) in thermal diffusivity, depending on grain orientation – reasonably similar to our calculated difference of 2.3 mm^2/s for unirradiated L x T orientation material. Generally, the unirradiated and irradiated specimens exhibit similar diffusivity whether calculated from resistivity measurements or measured directly. Dose and temperature differences, however, make exact comparison difficult. It should also be noted that laser flash method should expect ~5% error at room temperature [42].

Comparing SCW data from this work, we see reasonably similar values between doses and temperatures between the measured and fitted α and the calculated α_e. The only exception to this is in the low-temperature, low-dose instance. Here, the calculated α_e is much higher than measured α. We attribute this discrepancy to either the lower

Table 6
Comparison of measured/fitted thermal diffusivity values, α, and electronic contribution to the thermal diffusivity, α_e calculated with a Lorenz number of 3.2 • 10^{-8} WΩK^{-2}. Uncertainty given in α_e is one standard deviation. Data attributed to Akiyoshi can be found in [34]. Orientation defines whether elongated grains are perpendicular or parallel to the direction of heat or electron flow.

Sample ID	Dose (dpa)	Irrad. Temp (°C)	Orientation	Measurement fit α at room temp (mm^2/s)	Calculated α_e at 20 °C (mm^2/s)	Refs.
BT no irrad	0	–	⊥		69.5 ± 2.1	Present work
4003	0	–	⊥	70.8		[34]
BT no irrad	0	–	‖		71.8 ± 1.9	Present work
500H	0	–	‖	73.8		[34]
BT02	0.38	590	⊥		55.2 ± 2.1	Present work
4000	0.46	660	⊥	58.0		[34]
BT02	0.38	590	‖		58.3 ± 2.0	Present work
5001	0.25	550	‖	58.5		[34]
Sample ID	**Dose (dpa)**	**Irrad. Temp (°C)**	**Orientation**	**Measurement fit α at 20 °C (mm^2/s)**	**Calculated α_e at 20 °C (mm^2/s)**	**Reference**
UE no irrad	0	–	–		74.7 ± 2.4	Present work
UE no irrad 2	0	–	–	69.7		Present work
UE02	0.30	550	–		66.0 ± 9.8	Present work
UE03	0.26	480	–	54.0		Present work
UE05	0.71	810	–		55.6 ± 8.6	Present work
UE0G	0.74	830	–	55.6		Present work
UE06	0.70	990	–		58.9 ± 1.8	Present work
UE0L	0.63	930	–	55.6		Present work

irradiation temperature of UE03 (and therefore the effect of Frenkel pairs creating some deviation from Wiedemann-Franz) or the particularly large data spread for the resistivity of this sample (see Fig. 6), which is attributed to machining artefacts from EDM, which were much more severe on the SCW samples. Because we find such similarity between measured α and calculated α_e, for similar doses on identical materials, we cannot show any systematic deviation from Wiedemann–Franz. Therefore, we assume that Wiedemann–Franz holds for neutron-irradiated tungsten at the measured doses/temperatures.

4.3. Effect of rhenium content

Electrical resistivity evolution in neutron irradiated tungsten has been recently studied by Tanno et al. [39] (≤1.54dpa, ≤740 °C, irradiated in the Joyo fast reactor), Hasegawa et al. [15] (0.15–1.0 dpa at around 500–600 °C), and Mergia et al. [29] (0.18dpa, ≤1200 °C, irradiated with steel shielding in the fuel element of BR2). The change in resistivity (induced either by addition of *Re* during alloying (other authors) or neutron irradiation in HFIR (present work)) is plotted against reported dpa for similar temperatures in Fig. 8. A single pre-alloyed, irradiated sample - 410F (W3%*Re*, shown in orange) measures the changed resistivity against unalloyed, unirradiated PCW – effectively adding both irradiation and alloying effects.

Resistivity contributions from transmutation impurities in solid solution can be calculated using Matthiessen's rule with Tanno's [39] calculated impurity parameters, *I*, and the impurity content, x, in% at. This parameter can be calculated separately for each constituent, but is only done for *Re* in this work using Tanno's impurity parameter of 145 for *Re* in W.

$$\rho_{tr.SS} = Ix(1-x) \tag{6}$$

No studies which quantify transmutation and resistivity following neutron irradiation were identified for inclusion into Fig. 8. However, in neutron irradiated tungsten (both in samples from this irradiation [43] and elsewhere [36,44]), transmutant *Re* precipitates at the grain boundaries. In SCW samples, and far from grain boundaries, *Re* (and Os) precipitate into clusters at sufficient dose, rather than remaining in solid solution. As noted in Eq. (5):, transmutant elements in solid solution and precipitates are expected to behave differently. At doses higher than explored in this study, precipitation behavior will likely drive deviations from this approximation curve.

From the TEM data on samples from this irradiation campaign [43], we know that the highest-dose SCW samples experience concentration of transmutant elements around voids, while the PCW specimens do not exhibit this behavior at the same levels, but may experience segregation to the GBs. We posit, therefore, that our PCW samples exhibit transmutation effects which cause increases in resistivity due to lattice changes from solid-solution and GBs but not precipitates, while the SCW samples exhibit transmutant solid solution and precipitation effects, but not GBs.

4.4. Grain boundary and matrix resistivity

Resistivity as a function of GB density – in the direction of the current – is shown in Fig. 9A) for three samples with elongated grains which were rotated to achieve different GB densities (see the top row of Fig. 5). GBs present a natural scattering site for electrons. In addition, studies have shown [37,45], Re enrichment will occur at GBs in irradiated W. Any such enrichment necessitates electrons cross a Re-enriched zone, while Re pre-clusters and clusters may be bypassed elsewhere and in SCW. Assuming the effect of grain boundaries scales linearly with GB density, the slope of the line in Fig. 9A) can be taken as the GB effect on resistivity. There is an observed increasing slope trend (from 0.4 to 0.6 $\frac{\mu\Omega \bullet cm}{GB/\mu m}$ per at% Re) with increasing dose/Re content. The uncertainty thresholds in resistivity, however, make this trend difficult to quantify precisely and would benefit from future study.

From the discussion in 4.4, we suspect that the degradation of the GB effects in PCW is due to segregation of Re to the GBs. We, therefore, attribute the changes to the resistivity slope to Re segregation to the GBs.

We can build an expression for grain boundary resistivity from work performed by Andrews et al. [46,47], which has recently been explored in conjunction with Matthiessen's rule by Bakonyi [48]. Andrews et al.'s work assumes spherical grains, however, which are not the case for this work. Geometrically, we assume that all grains can be treated as ellipsoids with perpendicular radii of a, b, and c in the x, y, and z axes, respectively. We define the direction of the current to be in the z-direction. Considering only net electron motion in the direction of the current, the mean distance encountered between grain boundary encounters will be the average height, z, of the ellipsoid. This can be derived by doubling the mean chord length of the positive octant of an ellipsoid centered on the origin, where A represents the cross-sectional area of the ellipse in the x-y plane.

$$Mean(z) = 2\cdot\frac{1}{\frac{1}{4}A}\iint z(x,y)dydx = 2\cdot\frac{1}{\frac{1}{4}A}\int_0^a\int_0^{b\sqrt{1-\frac{x^2}{a^2}}} c\sqrt{1-\frac{x^2}{a^2}-\frac{y^2}{b^2}}\,dy\,dx = \frac{4}{3}c \tag{7}$$

Conveniently, this is the same result as the spherical case explored by Andrews et al. [47]. Therefore, we can proceed to approximate GB

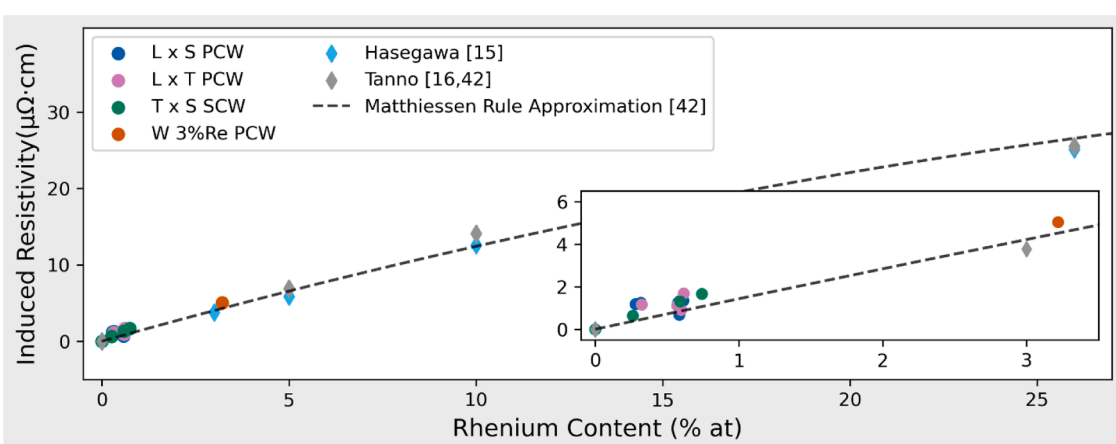

Fig. 8. Comparison of recent resistivity/neutron irradiation studies with this work. Work from Tanno et al. [16,39]. and Hasegawa et al. [15]. are for unirradiated material. The fit dashed line displayed is derived from Tanno's calculations of impurity parameters for Matthiessen's rule.

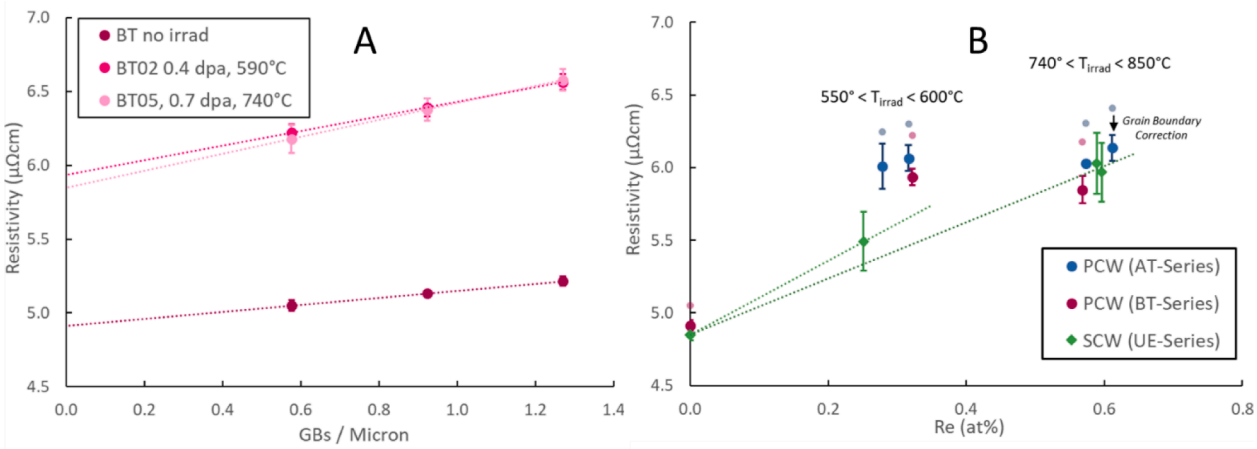

Fig. 9. (A) Resistivity for oscillatory BT-series samples as a function of GB density. (B) PCW resistivity values minus the calculated GB effect from part A are compared with SCW. Original, as-measured PCW shown with smaller, lighter markers. Uncertainty bars are standard deviation.

resistivity effects with the simple expression:

$$\rho_{GB} + \rho_{tr.GB} = \frac{A}{d} \tag{8}$$

Here, d is the diameter of the grain in the direction of the current, (replacing c, which was used above, for an easier to understand convention) and A is the Andrews parameter (a proportionality factor equal to the slope of the lines in Fig. 9A). Resistivity attributed to GBs and calculated values for A are shown alongside calculated *Re* content and extrapolated resistivity for the zero-GB condition in Table 7.

When considering the matrix effects observed in Fig. 9B), we note good agreement between the calculated matrix resistivity from PCW samples and observed resistivity from the SCW samples. The only exception to this is in the 550–600 °C irradiations, where the SCW samples appear to have lower resistivity than the calculated matrix values. It is unclear what this is attributable to. Two possible explanations include: (1) the fact that we only have a single SCW sample, which itself has a large uncertainty, gives a misleading impression or (2) GBs inhibiting self-interstitial migration to a greater degree than acting as an interstitial sink.

4.5. Textural effects

Textural effects could provide an alternate explanation for the observed oscillatory effects in measurements. Zakharova et al. [17] reported electrical resistivity values for SCW, measured at 25 °C, for the [100], [110], and [111] directions. The samples were measured again after neutron irradiation at 460 °C in BR-10 to fluences of 1.14×10^{26} n/m^2 ($E > 0.1$ MeV) – roughly triple the highest dose from this work of 0.37×10^{26} n/m^2 ($E > 0.1$ MeV). Their results, reproduced in Table 8, indicate a maximum textural difference of 0.07 μΩ•cm before irradiation and 0.24 μΩ•cm after irradiation.

Because we would expect texture to have - at absolute maximum - an effect of 3.7%, observe oscillatory effects as high as 6.1%, and do not observe oscillation in the rotation of SCW samples (to within our measurement limits), we do not find texture to be an adequate explanation to observed oscillation.

Table 8
SCW orientation effects reported by Zakharova et al. [17].

	[100]	[110]	[111]	Max Difference	Relative effect
Unirradiated ρ (μΩ•cm)	5.62	5.55	5.62	0.07	1.2%
Irradiated @ 900 °C ρ (μΩ•cm)	6.57	6.33	6.38	0.24	3.7%
Irradiated @ 900 °C Annealed ρ (μΩ•cm)	6.45	6.30	6.33	0.15	2.3%

4.6. Attribution of specific irradiation effects on resistivity degradation

From Eq. (5), we have been able to measure or estimate values for lattice resistivity ($\rho_{lattice}$), the effects of GBs (ρ_{GB}) together with transmutant segregation to GBs ($\rho_{tr.GB}$), and solid-solution transmutation ($\rho_{tr.SS}$). For our dose and temperature regime, we observe no evidence of transmutant precipitates in the bulk ($\rho_{tr.P}$) and assume no significant textural effects (ρ_{tex}). Void (ρ_{void}), dislocation (ρ_{dis}), vacancy (ρ_v), and interstitial effects (ρ_i) are at least partially annealed out at the highest temperature irradiations. Therefore, the sum of these four effects should be inversely proportional to irradiation temperature and proportional to dose until/unless saturation of defects occurs. This sum (termed ρ_{temp} for the inverse relationship to irradiation temperature) can be quantified by subtracting the quantified effects from the observed resistivity ($\rho_{observed}$). Calculated values are show in Table 9.

$$\rho_{temp} = \rho_{void} + \rho_{dis} + \rho_v + \rho_i = \rho_{observed} - \rho_{lattice} - \rho_{GB} - \rho_{tr.SS} - \rho_{tr.GB} \tag{9}$$

We conclude from these calculations that – for the polycrystalline samples – the combined resistivity degradation from voids, dislocations, vacancies, and interstitials is likely greater than that from solid state transmutation at lower (~590 °C) irradiation temperatures. This trend reverses at higher temperature irradiation, where mobile lattice defects can anneal out, and the solid solution transmutation becomes the dominant factor at higher temperatures (shown here in the temperatures ≥740 °C).

Table 7
Irradiation condition, resistivity range attributed to GB effects, Andres Parameter, calculated Re content, and calculated zero-GB resitivities for selected samples.

Irradiation Condition	ρ_{GB} ($\Delta\rho_{GB}$) (μΩ•cm)	Relative effect	Andrews Parameter (μΩ•cm/GB/μm)	Calculated Re (at%)	Zero-GB ρ (μΩ•cm)
SCW no irradiation	–	–	–	–	4.9
L x T no irradiation	0.14–0.30 (0.17)	3.2%	0.24	0	4.9
L x T 0.4 dpa / 590 °C	0.28–0.63 (0.34)	5.2%	0.49	0.4%	5.9
L x T 0.7 dpa / 740 °C	0.33–0.73 (0.40)	6.1%	0.58	0.8%	5.8

Table 9
Calculated resistivity contributions to observed resistivity. L x T face samples use directly calculated Andrews parameters. GB contributions for L x S face samples irradiated at similar conditions are calculated with identical Andrews parameters. Resistivity values are μΩ•cm.

Irradiation Condition	Sample ID	Re (% at)	$\rho_{observed}$	$\rho_{lattice}$	$\rho_{GB}+\rho_{tr.GB}$	$\rho_{tr.SS}$	ρ_{temp}
SCW no irradiation	UE no irrad	–	4.85	4.85	–	–	–
SCW 0.3 dpa / 480 °C	UE02	0.26%	5.49	4.85	–	0.38	0.27
SCW 0.7 dpa / 830 °C	UE05	0.74%	5.97	4.85	–	1.07	0.05
L x T no irradiation	BT no irrad	–	5.05	4.85	0.14	–	–
L x T 0.4 dpa / 590 °C	BT02	0.32%	6.22	4.85	0.28	0.47	0.62
L x T 0.7 dpa / 740 °C	BT05	0.57%	6.18	4.85	0.33	0.82	0.18
L x S 0.4 dpa / 590 °C	AT01	0.32%	6.30	4.85	0.24	0.46	0.76
L x S 0.7 dpa / 760 °C	AT05	0.57%	6.30	4.85	0.27	0.83	0.35

5. Summary and conclusions

Electrical resistivity and thermal diffusivity measurements have been taken for neutron irradiated W and W-3%*Re* with *Re* transmutation rates similar to what is expected in fusion reactors. Materials were irradiated to doses between 0.3 and 0.9 dpa at temperatures ranging from 550 to 990 °C and changes to resistivity have been reported. Based on the literature, a mathematical description of irradiation effects on electron transport has been presented. We conclude that:

- Electrical resistivity varies with grain boundary density in respect to the direction of the applied current. This variation has been quantified with respect to grain size. Andrews parameters (which can be used to calculate grain boundary contributions for arbitrary grain sizes) have been calculated for unirradiated W and W irradiated at these conditions. Increasing irradiation dose appears to increase the Andrews parameter.
- For samples irradiated to 0.4 dpa near 590 °C (below the vacancy migration threshold around 650 °C), the combined resistivity degradation due to voids, vacancies, interstitials, and dislocations is estimated to be greater than the contribution from solid solution *Re* transmutation, which in turn is greater than the contribution from grain boundaries. At doses 0.7 dpa near 750 °C, solid solution *Re* contributions to resistivity degradation are greater than all other effects combined. In the no-irradiation case and doses/temperatures near 0.7 dpa / 750 °C, observed SCW resistivity and the adjusted PCW matrix resistivity with these Andrews parameters are similar.
- Based on thermal diffusivity and electrical resistivity data, the Wiedemann–Franz law appears to hold for tungsten under irradiation for the measured conditions.
- Grain growth has been observed and quantified for our irradiation conditions – mean aerial growth rates of 0.5 μm^2 (550 °C/0.29 dpa) and 1.2 μm^2 (870 °C/0.74 dpa) for the tested microstructure. Recrystallization has also been observed in high temperature (~990 °C) irradiations.

Declaration of Competing Interest

The authors declare that they have no known competing financial interests or personal relationships that could have appeared to influence the work reported in this paper.

Acknowledgments

The authors would like to thank Stephanie Curlin, Hsin Wang, Ricardo Muse, and Brandon Hambrick.

The work was performed as a part of the U.S.-Japan PHENIX Cooperation Project on Technological Assessment of Plasma Facing Components for DEMO Reactors, supported by the U.S. Department of Energy (DOE), Office of Science, Fusion Energy Sciences and Ministry of Education, Culture, Sports, Science and Technology, Japan. This manuscript has been authored by UT-Battelle, LLC, under contract number DE-AC05–00OR22725 with the DOE. This research used resources at the HFIR, a DOE Office of Science User Facility operated by ORNL. This work was supported in part by the Oak Ridge Institute for Science and Education under the Nuclear Engineering Science Laboratory Synthesis program. Dr. Echols would also like to acknowledge EPSRC Grant is EP/W006839/1.

Supplementary materials

Supplementary material associated with this article can be found, in the online version, at doi:10.1016/j.actamat.2023.119025.

References

[1] A.F. Rowcliffe, L.M. Garrison, Y. Yamamoto, L. Tan, Y. Katoh, Materials challenges for the fusion nuclear science facility, Fusion Eng. Des. 135 (2018) 290–301, https://doi.org/10.1016/j.fusengdes.2017.07.012.
[2] C.E. Kessel, J.P. Blanchard, A. Davis, L. El-Guebaly, L.M. Garrison, N.M. Ghoniem, P.W. Humrickhouse, Y. Huang, Y. Katoh, A. Khodak, E.P. Marriott, S. Malang, N. B. Morley, G.H. Neilson, J. Rapp, M.E. Rensink, T.D. Rognlien, A.F. Rowcliffe, S. Smolentsev, L.L. Snead, M.S. Tillack, P. Titus, L.M. Waganer, G.M. Wallace, S. J. Wukitch, A. Ying, K. Young, Y. Zhai, Overview of the fusion nuclear science facility, a credible break-in step on the path to fusion energy, Fusion Eng. Des. 135 (2018) 236–270, https://doi.org/10.1016/j.fusengdes.2017.05.081.
[3] Y. Chen, J. Ma, W. Li, Understanding the thermal conductivity and Lorenz number in tungsten from first principles, Phys. Rev. B 99 (2019), https://doi.org/10.1103/PhysRevB.99.020305.
[4] J.P. Crocombette, P. Notargiacomo, M.C. Marinica, Effect of the variation of the electronic density of states of zirconium and tungsten on their respective thermal conductivity evolution with temperature, J. Phys. Condens. Matter 27 (2015), 165501, https://doi.org/10.1088/0953-8984/27/16/165501.
[5] L. Hu, B.D. Wirth, D. Maroudas, Thermal conductivity of tungsten: effects of plasma-related structural defects from molecular-dynamics simulations, Appl. Phys. Lett. 111 (2017), 081902, https://doi.org/10.1063/1.4986956.
[6] B. Fu, W. Lai, Y. Yuan, H. Xu, W. Liu, Calculation and analysis of lattice thermal conductivity in tungsten by molecular dynamics, J. Nucl. Mater. 427 (2012) 268–273, https://doi.org/10.1016/j.jnucmat.2012.05.015.
[7] T. Tanabe, C. Eamchotchawalit, C. Busabok, S. Taweethavorn, M. Fujitsuka, T. Shikama, Temperature dependence of thermal conductivity in W and W–Re alloys from 300 to 1000K, Mater. Lett. 57 (2003), https://doi.org/10.1016/S0167-577X(02)01403-9.
[8] B. Fu, W. Lai, Y. Yuan, H. Xu, W. Liu, Calculation and analysis of lattice thermal conductivity in tungsten by molecular dynamics, J. Nucl. Mater. (2012) 427, https://doi.org/10.1016/j.jnucmat.2012.05.015.
[9] J.A.H. Littleton, R.A. Secco, W. Yong, M. Berrada, Electrical resistivity and thermal conductivity of W and Re up to 5 GPa and 2300 K, J. Appl. Phys. 125 (2019), https://doi.org/10.1063/1.5066103.
[10] Y. Katoh, L.L. Snead, L.M. Garrison, X. Hu, T. Koyanagi, C.M. Parish, P. D. Edmondson, M. Fukuda, T. Hwang, T. Tanaka, A. Hasegawa, Response of unalloyed tungsten to mixed spectrum neutrons, J. Nucl. Mater. 520 (2019) 193–207, https://doi.org/10.1016/j.jnucmat.2019.03.045.
[11] L.K. Keys, J.P. Smith, J. Moteff, High-temperature recovery of tungsten after neutron irradiation, Phys. Rev. 176 (1968), https://doi.org/10.1103/PhysRev.176.851.
[12] H.H. Neely, D.W. Keefer, A. Sosin, Electron irradiation and recovery of tungsten, Phys. Status Solidi (b) (1968) 28, https://doi.org/10.1002/pssb.19680280225.
[13] M.W. Thompson, The damage and recovery of neutron irradiated tungsten, Philos. Mag. 5 (1960) 278–296, https://doi.org/10.1080/14786436008235842.
[14] M.S. Anand, B.M. Pande, R.P. Agarwala, Recovery in neutron irradiated tungsten, Radiat. Eff. 39 (1978) 149–155, https://doi.org/10.1080/00337577808234468.
[15] A. Hasegawa, T. Tanno, S. Nogami, M. Satou, Property change mechanism in tungsten under neutron irradiation in various reactors, J. Nucl. Mater. (2011) 491–494, https://doi.org/10.1016/j.jnucmat.2010.12.114.
[16] T. Tanno, A. Hasegawa, M. Fujiwara, J.C. He, S. Nogami, M. Satou, T. Shishido, K. Abe, Precipitation of solid transmutation elements in irradiated tungsten alloys, Mater. Trans. 49 (2008) 2259–2264, https://doi.org/10.2320/matertrans.MAW200821.

[17] M.I. Zakharova, N.A. Artemov, V.v. Bogdanov, Effects of neutron irradiation and annealing on the elastic moduli and electrical resistivity of molybdenum and tungsten single crystals, Inorg. Mater. 37 (2001) 786–789, https://doi.org/10.1023/A:1017979230262.
[18] Y. Katoh, D. Clark, Y. Ueda, Y. Hatano, M. Yoda, A.S. Sabau, T. Yokomine, L. M. Garrison, J.W. Geringer, A. Hasegawa, T. Hinoki, M. Shimada, D. Buchenauer, Y. Oya, T. Muroga, Progress in the U.S./Japan PHENIX project for the technological assessment of plasma facing components for DEMO reactors, Fusion Sci. Technol. 72 (2017) 222–232, https://doi.org/10.1080/15361055.2017.1333868.
[19] J.W. Geringer, J.L. McDuffee, C.M. Petrie, L.M. Garrison, R.H. Howard, N.O. Cetiner, D.A. Stringfield, R.G. Sitterson, 10.4 HFIR-MFE-RB-19J specimen loading listing, 2016.
[20] L.M. Garrison, Y. Katoh, N. Reid, E. Proehl, M. Fukuda, 4.6 microstructure and mechanical properties of irradiated phenix program tungsten, 2017.
[21] M.E. Sawan, Transmutation of tungsten in fusion and fission nuclear environments, Fusion Sci. Technol. 66 (2014), https://doi.org/10.13182/FST13-717.
[22] T. Noda, M. Fujita, M. Okada, Transmutation and induced radioactivity of W in the armor and first wall of fusion reactors, J. Nucl. Mater. (1998) 258–263, https://doi.org/10.1016/S0022-3115(98)00088-9.
[23] L.M. Garrison, Y. Katoh, J.W. Geringer, M. Akiyoshi, X. Chen, M. Fukuda, A. Hasegawa, T. Hinoki, X. Hu, T. Koyanagi, E. Lang, M. McAlister, J. McDuffee, T. Miyazawa, C. Parish, E. Proehl, N. Reid, J. Robertson, H. Wang, PHENIX U.S.-Japan, Collaboration investigation of thermal and mechanical properties of thermal neutron–shielded irradiated tungsten, Fusion Sci. Technol. 75 (2019), https://doi.org/10.1080/15361055.2019.1602390.
[24] L.R. Greenwood, B.D. Pierson, T. Trang-Le, 11.4 HFIR-MFE-RB-19J neutron fluence measurements and radiation damage calculations (REVISED), 2019.
[25] T. Noda, M. Fujita, M. Okada, Transmutation and induced radioactivity of W in the armor and first wall of fusion reactors, J. Nucl. Mater. (1998) 258–263, https://doi.org/10.1016/S0022-3115(98)00088-9.
[26] M.E. Sawan, Transmutation of tungsten in fusion and fission nuclear environments, Fusion Sci. Technol. 66 (2014), https://doi.org/10.13182/FST13-717.
[27] J.L. McDuffee, C.R. Daily, N.O. Cetiner, C.M. Petrie, J.W. Geringer, 10.3 HFIR-MFE-RB-19J Thermal and Neutronic Design, 2016.
[28] J.H. You, M. Li, K. Zhang, Structural lifetime assessment for the DEMO divertor targets: design-by-analysis approach and outstanding issues, Fusion Eng. Des. 164 (2021), 112203, https://doi.org/10.1016/j.fusengdes.2020.112203.
[29] J.P. Blanchard, C. Martin, Thermomechanical analysis for an all-tungsten ARIES Divertor, Fusion Sci. Technol. 67 (2015) 158–166, https://doi.org/10.13182/FST14-796.
[30] J. McDuffee, T. Daly, Experimental and computational study of the flux spectrum in materials irradiation facilities of the high flux isotope reactor, in: PHYSOR 2012 - Advances in Reactor Physics - Linking Research, Industry, and Education, 2012.
[31] A.A. Campbell, W.D. Porter, Y. Katoh, L.L. Snead, Method for analyzing passive silicon carbide thermometry with a continuous dilatometer to determine irradiation temperature, Nucl. Instrum. Methods Phys. Res. B 370 (2016), https://doi.org/10.1016/j.nimb.2016.01.005.
[32] M.A. Logan, An AC bridge for semiconductor resistivity measurements using a four-point probe, 1961.
[33] ASTM B193-20, Standard Test Method For Resistivity of Electrical Conductor Materials, ASTM International, 2020.
[34] M. Akiyoshi, L.M. Garrison, J.W. Geringer, H. Wang, A. Hasegawa, S. Nogami, Y. Katoh, Thermal diffusivity of irradiated tungsten and tungsten-rhenium alloys, J. Nucl. Mater. 543 (2021), https://doi.org/10.1016/j.jnucmat.2020.152594.
[35] W. Pantleon, Thermal stability of the microstructure in rolled tungsten for fusion reactors, Phys. Scr. 96 (2021), 124036, https://doi.org/10.1088/1402-4896/ac2854.
[36] X. Hu, C.M. Parish, K. Wang, T. Koyanagi, B.P. Eftink, Y. Katoh, Transmutation-induced precipitation in tungsten irradiated with a mixed energy neutron spectrum, Acta Mater. 165 (2019) 51–61, https://doi.org/10.1016/j.actamat.2018.11.032.
[37] T. Koyanagi, N.A.P.K. Kumar, T. Hwang, L.M. Garrison, X. Hu, L.L. Snead, Y. Katoh, Microstructural evolution of pure tungsten neutron irradiated with a mixed energy spectrum, J. Nucl. Mater. 490 (2017) 66–74, https://doi.org/10.1016/j.jnucmat.2017.04.010.
[38] L.M. Garrison, Y. Katoh, N.A.P.K. Kumar, Mechanical properties of single-crystal tungsten irradiated in a mixed spectrum fission reactor, J. Nucl. Mater. 518 (2019), https://doi.org/10.1016/j.jnucmat.2019.02.050.
[39] T. Tanno, A. Hasegawa, J.C. He, M. Fujiwara, M. Satou, S. Nogami, K. Abe, T. Shishido, Effects of transmutation elements on the microstructural evolution and electrical resistivity of neutron-irradiated tungsten, J. Nucl. Mater. 386 (388) (2009) 218–221, https://doi.org/10.1016/j.jnucmat.2008.12.091.
[40] K. Mergia, V. Chatzikos, E. Manios, S. Dellis, D. Papadakis, D. Terentyev, G. Bonny, A. Dubinko, I.E. Stamatelatos, S. Messoloras, M. Rieth, Evolution of microstructure in neutron irradiated cold rolled tungsten and its correlation with hardness, Fusion Eng. Des. 172 (2021), 112784, https://doi.org/10.1016/j.fusengdes.2021.112784.
[41] A. Reza, H. Yu, K. Mizohata, F. Hofmann, Thermal diffusivity degradation and point defect density in self-ion implanted tungsten, Acta Mater. 193 (2020) 270–279, https://doi.org/10.1016/j.actamat.2020.03.034.
[42] ASTM E1461-13: Standard test method for thermal diffusivity by the flash method, 2016.
[43] D. Morrall, J. Echols, J. Geringer, C. Parish, L. Garrison, Void swelling and transmutation in tungsten metals and alloys after fusion relevant neutron irradiation, in: Proceedings of the 18th International Conference on Plasma-Facing Materials and Components for Fusion Applications, 2021.
[44] R.K. Williams, F.W. Wiffen, J. Bentley, J.O. Stiegler, Irradiation induced precipitation in tungsten based, W-Re alloys, Metall. Trans. A 14 (1983) 655–666, https://doi.org/10.1007/BF02643781.
[45] M. Dürrschnabel, M. Klimenkov, U. Jäntsch, M. Rieth, H.C. Schneider, D. Terentyev, New insights into microstructure of neutron-irradiated tungsten, Sci. Rep. 11 (2021) 7572, https://doi.org/10.1038/s41598-021-86746-6.
[46] P.V. Andrews, Resistivity due to grain boundaries in pure copper, Phys. Lett. 19 (1965), https://doi.org/10.1016/0031-9163(65)90776-6.
[47] P.v. Andrews, M.B. West, C.R. Robeson, The effect of grain boundaries on the electrical resistivity of polycrystalline copper and aluminium, Philos. Mag. 19 (1969), https://doi.org/10.1080/14786436908225855.
[48] I. Bakonyi, Accounting for the resistivity contribution of grain boundaries in metals: critical analysis of reported experimental and theoretical data for Ni and Cu, Eur. Phys. J. Plus 136 (2021) 410, https://doi.org/10.1140/epjp/s13360-021-01303-4.